Zoology 135 (2019) 125678

Contents lists available at ScienceDirect

Zoology

journal homepage: www.elsevier.com/locate/zool

The role of an overlooked adductor muscle in the feeding mechanism of ray-finned fishes: Predictions from simulations of a deep-sea viperfish

Christopher P. Kenaley[a,*], Mikhaila C. Marecki[b], George V. Lauder[b]

[a] Department of Biology, Boston College, 140 Commonwealth Avenue, Chestnut Hill, MA 02467, USA
[b] Museum of Comparative Zoology, Harvard University, 26 Oxford Street, Cambridge, MA 02138, USA

ARTICLE INFO

Keywords:
Dynamic model
Organismal design
Muscle dynamics
Steering motor
Bite force
Prey capture

ABSTRACT

In a majority of ray-finned fishes (Actinopterygii), effective acquisition of food resources is predicated on rapid jaw adduction. Although the musculoskeletal architecture of the feeding system has been the subject of comparative research for many decades, individual contributions of the major adductor divisions to closing dynamics have not been elucidated. While it is understood that the dorsal divisions that arise from the head and insert on the posterior of the lower jaw are major contributors to closing dynamics, the contribution of the ventral components of the adductor system has been largely overlooked. In many ray-finned fishes, the ventral component is comprised of a single division, the A_ω, that originates on an intersegmental aponeurosis of the facialis divisions and inserts on the medial face of the dentary, anterior to the Meckelian tendon. This configuration resembles a sling applied at two offset points of attachment on a third-order lever. The goal of this study was to elucidate the contributions of the A_ω to jaw adduction by modeling jaw closing in the deep-sea viperfish *Chauliodus sloani*. To do this, we simulated adduction with a revised computational model that incorporates the geometry of the A_ω. By comparing results between simulations that included and excluded A_ω input, we show that the A_ω adds substantially to lower-jaw adduction dynamics in *C. sloani* by acting as a steering motor and displacing the line of action of the dorsal facialis adductor muscles and increasing the mechanical advantage and input moment arms of the jaw lever system. We also explored the effect of the A_ω on muscle dynamics and found that overall facialis muscle shortening velocities are higher and normalized force production is lower in simulations including the A_ω. The net effect of these changes in muscle dynamics results in similar magnitudes of peak power in the facialis divisions between simulations, however, peak power is achieved earlier in adduction Modifications of muscle mechanics and posture result in significant increases in closing performance, including static bite force, angular velocity, and adduction time. We compare this configuration to a similar design in crocodilians and suggest that the A_ω configuration and similar sling configurations across the vertebrate tree of life indicate the importance of this musculoskeletal design in feeding.

1. Introduction

The oral jaw system of actinopterygian fishes is a highly kinetic and complex musculoskeletal system. Although feeding behavior may vary considerably between groups of fishes along a ram-suction continuum (Wainwright et al., 2015), a feeding event typically ends in a rapid adduction of the lower jaw to close the oral cavity (Westneat, 2005). Especially among predatory fishes that feed on large and elusive prey items, fast adduction reduces the chance of prey escape and increases the likelihood of prey capture success (Wainwright and Richard, 1995; Westneat, 2005).

In ray-finned fishes, the adductor mandibulae muscles power jaw closing. This complex is comprised of multiple divisions: the A_1, A_2, A_3, and A_ω (Winterbottom, 1973; although for an alternative nomenclature, see Datovo and Vari, 2013). The A_1 is the most dorsal section and typically inserts on the maxilla of the upper jaw. The A_2, originates on several bones of the suspensorium and typically inserts on the dentary at the coronoid process or within the Meckelian fossa (Winterbottom, 1973). The A_3 is the most medial of the four divisions and originates on ventral elements of the suspensorium and inserts on the medial face of the dentary, in the Meckelian fossa or both in some teleosts (Winterbottom, 1973). In many groups of teleosts, including the stomiid dragonfishes, the A_2 and A_3 share a tendinous insertion on the dentary via the Meckelian tendon (Fig. 1A and B; Datovo and Vari, 2013). Together, the A_1, A_2, and A_3 form the facialis segments of the adductor mandibulae.

* Corresponding author.
E-mail address: kenaley@bc.edu (C.P. Kenaley).

https://doi.org/10.1016/j.zool.2019.02.005
Received 17 July 2018; Received in revised form 13 February 2019; Accepted 25 February 2019
Available online 18 April 2019

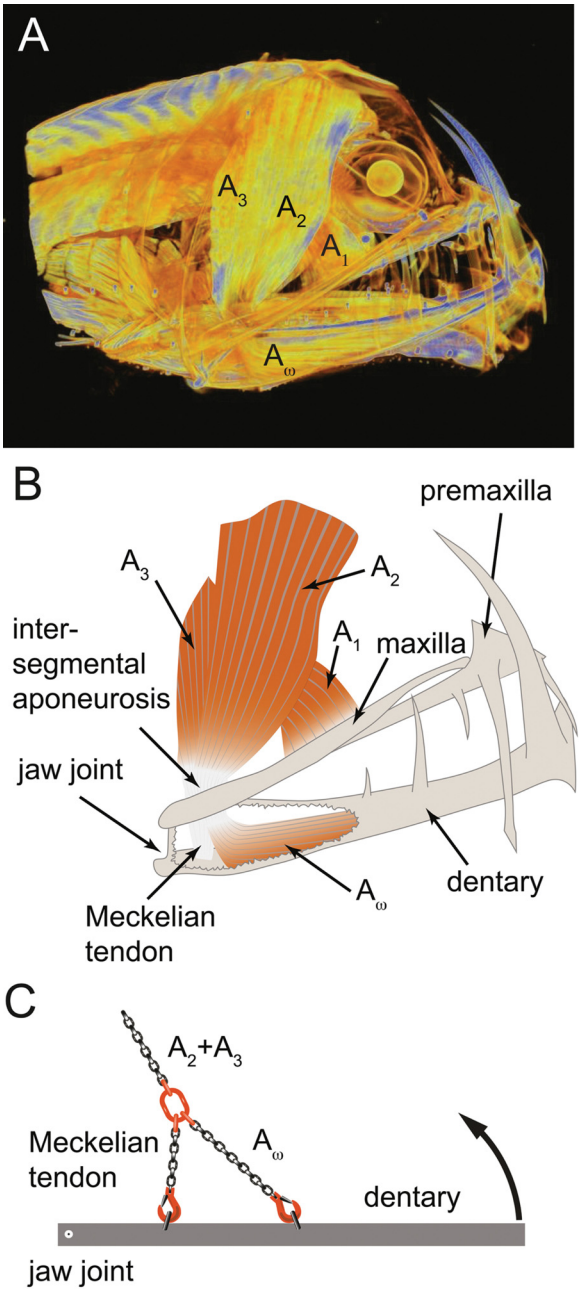

Fig. 1. Musculoskeletal architecture of the feeding system of the viperfish, *Chauliodus sloani*. (A) 3-D μ-CT reconstruction of the head and cranial musculature. Specimen in A was soaked in 0.3% phosphomolybdic acid prior to scanning to reveal *in-situ* muscle anatomy. (B) Schematic of the musculoskeletal components of the lower-jaw adduction system. An area of the posterior mandible was cut away to reveal the insertion position of the A_ω in the Meckelian fossa. (C) An analogy for the adductor-jaw system in *C. sloani*: a two-leg rigging sling with offset anchor points applied to a beam that is allowed to rotate at one end.

As the most ventral division, the A_ω typically inserts on the medial face of the dentary and originates on the intersegmental aponeurosis via the mandibular tendon (Fig. 1; Datovo and Vari, 2013). While some fishes lack the A_ω altogether (e.g., acanthuriforms, anguilliforms, gonorynchiforms, siluriforms and tetraodontiforms), it is present in various configurations in most teleost groups (Datovo and Vari, 2013). While the facialis components often comprise myriad configurations, the A_ω is rather simple in architecture in that it is either a single, non-pennate segment or subdivided into typically two subsegments, the dorsal coronalis and ventral mentalis sections (Datovo and Vari, 2013). The non-pennate condition is represented in many fishes, including elopomorphs, osteoglossomorphs, clupeiforms, and ostariophysians (Datovo and Vari, 2013), and at least some stomiiforms, including viper and dragonfishes (Fig. 1; Kenaley, 2012).

The geometric configuration of the lower jaw and adductor system thus resembles a two-leg rigging sling with offset anchor points applied to a beam that is allowed to rotate at one end (Fig. 1C). The two anchor points are represented by the anterior insertion of the A_ω and more posterior insertion of the Meckelian tendon (Fig. 2B and C). Under this scenario, the input load from the adductors will be applied to an anterior and posterior inlever of a third-order lever, torques that will be resisted by the negative torques and inertia of the outlever. If the input torques overcome the inertia of the lower jaw, it will be accelerated.

Although many studies have examined the overall role of the teleost adductor divisions in applying a torque to the lower jaw so that it rotates and closes about the mandibular joint (Lauder, 1980; Lauder and Norton, 1980; Gibb, 1995), few have assessed the relative contribution and comparative functionality of the geometries of this complex system (Van Wassenbergh et al., 2005; de Schepper et al., 2008). Furthermore, to our knowledge, no study has examined the functional contribution of the A_ω. While several studies have assessed force contribution of the facial divisions (A_1, A_2, and A_3) according to lever models (Westneat, 2004; Van Wassenbergh et al., 2005; de Schepper et al., 2008; Grubich et al., 2012; Kenaley, 2012), for the most part, the force contribution of the A_ω remains unknown.

This muscle geometry is found in several groups of deep-sea fishes, including the Stomiidae (Winterbottom, 1973; Kenaley, 2012; Datovo and Vari, 2013) and thus may have a specific utility for taxa that inhabit this ecosystem. Stomiids represent the apex predators at meso- and bathypelagic depths and serve as key trophic mediators in the energy transfer between the mesopelagic zone to the bathypelagic zone (Sutton and Hopkins, 1996). Despite the extremely limited food resources at these oceanic depths (Herring, 2002), stomiids have undergone an exceptional radiation and represent the most diverse family-level taxon in the deep-sea (Fink, 1985; Kenaley et al., 2014). Much of this ecological and evolutionary success has no doubt been facilitated by their unique feeding morphologies (Kenaley, 2012). Perhaps most notable among these are long jaws that are studded with extremely long fang-like teeth (Fig. 1). In addition, the presence of an occipito-vertebral gap between the skull and the anteriormost vertebra allows dragonfishes to drastically rotate their neurocranium and thus open their jaws to an extremely large gape greater than > 120° (Tchernavin, 1953; Schnell et al., 2010; Kenaley, 2012; Schnell and Johnson, 2017). The large gape and fangs permit the ingestion of myctophid fishes that are typically 50% or more of the dragonfish's body length (Clarke, 1982; Sutton and Hopkins, 1996).

For this feeding behavior to be effective in the capture of relatively large and fast prey items like species of the family Myctophidae, the mandibles of *Chauliodus* and other stomiids must accomplish two tasks: (1) close quickly against the prey item and (2) apply enough force to immobilize or accelerate the bulky prey item toward the upper jaw. To accelerate the jaw, the adductor muscles must overcome resistive forces including inertia, intraoral pressure, and drag. Through two-dimensional computational dynamic modeling, de Schepper et al. (2008) suggested that high drag forces associated with long jaws may be overcome with increased physiological cross-sectional area (PCSA) of adductor muscles and that fast jaw adduction may be accomplished through a combination of relatively lower mechanical advantage and increased PCSA. The second task of producing bite forces high enough to immobilize and accelerate a prey item toward the upper jaw may also be facilitated by increased PCSA. However, Kenaley (2012) found that stomiids possess greatly reduced adductor masses and PCSA and proposed that this was an adaptation to the energy-poor deep sea and thus absolute magnitudes of bite force are extremely low.

All former studies addressing lower-jaw adduction in ray-finned

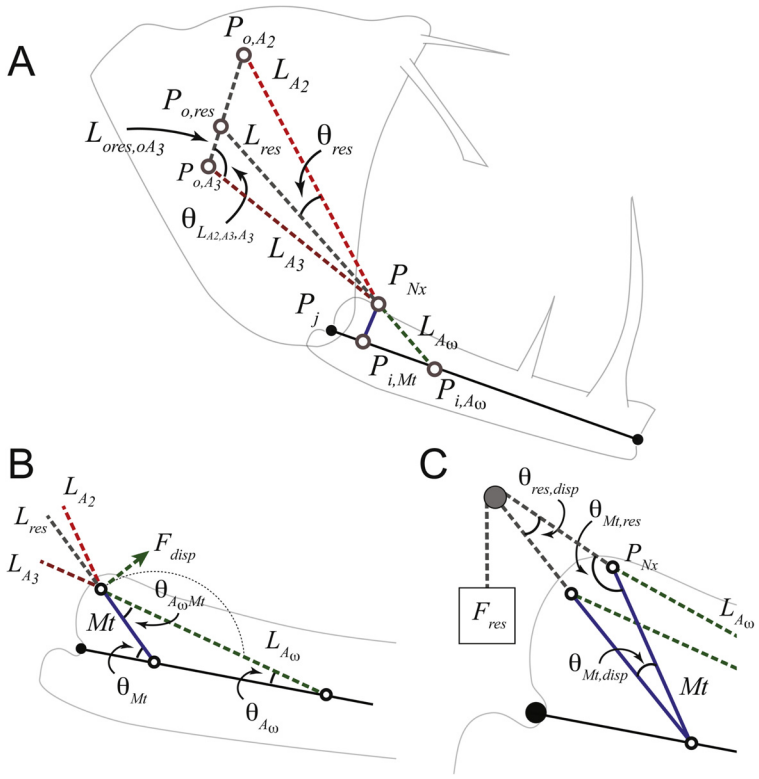

Fig. 2. Schematic diagram depicting muscle and tendon geometries (see Table 1 for abbreviations). (A) Lines of action and positions of the facialis adductors A_2 and A_3, their resultant, the origin of A_ω on the Meckelian tendon (*Mt*), and insertion of the A_ω on the lower jaw. Dashed lines in red, maroon, and green colors represent the lines of action of the A_2, A_3, and A_ω, respectively (L_{A_2}, L_{A_3}, and L_{A_ω}). Black line indicates the line of action of the facialis resultant. (B) Position of the nexus and adductor and tendon geometry before the force of A_ω is accounted for. Note that this is the tendon and muscle geometry in alternative simulations when the A_ω input is ignored. F_{disp} indicates the perpendicular force imposed by the A_ω on the Meckelian tendon and is equal to $F_{A_\omega} \times \sin(\theta_{A_\omega,Mt})$. The dashed arc indicates the possible position of P_{Nx} as it rotates about $P_{i,Mt}$ on the segment *Mt*. (C) The modeled effect of F_{disp} on the position of the Meckelian tendon and therefore P_{Nx}. The facialis resultant force (F_{res}) was modeled as if it were applied about a pulley at $P_{o,res}$ (note position of $P_{o,res}$ and L_{res} in C is not to scale). Under this scenario, F_{disp} and F_{res} resulted in the angles $\theta_{Mt,res}$ and $\theta_{res,disp}$ and thus the tendon experiences an angular displacement $\theta_{Mt,disp}$. Note that A represents the initial geometry at $t = 0$ for all three divisions.

fishes, including Kenaley (2012), have largely neglected the role of the A_ω. Consequently, a question arises: does the architecture of the two-anchor sling of *Chauliodus* play an important role in generating significant positive forces? The goals of this study were to elucidate the contributions of the A_ω in jaw-adduction in *Chauliodus* in particular and ray-finned fishes in general. Specifically, we set out to establish how the contribution of the A_ω and two-anchor sling affects feeding performance in terms of adduction duration, velocity, and force transmission. Furthermore, we set out to evaluate the potential of this system to change the lines of action of the facialis components. If the input of the A_ω does affect the lines of action, the potential also exists for the A_ω to alter the length of the facialis division and muscle dynamics during closing. Thus, we also sought to evaluate whether the A_ω could alter the position of the facialis divisions on their respective force-length and force-velocity curves and therefore substantially alter muscle power. To do this, we simulated jaw adduction in preserved specimens of *C. sloani* using a revised computational model developed for jaw adduction in stomiid dragonfishes by Kenaley (2012), one that incorporates the geometry of the A_ω.

2. Materials and methods

2.1. Morphometric data

All specimens were obtained from the Museum of Comparative Zoology, Harvard University. A total of ten preserved individuals of *Chauliodus sloani* were measured with standard lengths (SL) ranging from 10.3 cm to 25.8 cm. Each specimen was photographed and digitized according to Kenaley (2012). A summary of these measurements are given in Supplemental Table 1.

To better visualize *in-situ* muscle morphology, the head of a single specimen (MCZ 129265, 20.0 cm SL) was removed from the body, and soaked in 0.3% phosphomolybdic acid (PMA) for three days following Metscher (2009). After PMA application, the specimen was scanned in a SkyScan1173 high-energy spiral-scan μ-CT unit (MicroPhotonics, Inc., Allentown, PA). Scan parameter values for amperage, voltage, exposure time, and image rotation were 58 μ-A, 110 kV, 730 ms, and 0.7°, respectively. The scan produced a voxel size of 24 µm. After slice reconstruction in NRecon (Micro Photonics, Inc.), segmentation and volume rendering were performed in Mimics 15.0 (Materialise, Leuven, Belgium).

2.2. Jaw adduction model

Jaw-closing simulations were implemented in a custom R script (Team, 2018) that models lower-jaw adduction using a dynamic equilibrium model based on that of Van Wassenbergh et al. (2005) and Kenaley (2012). The R code is available on GitHub (https://github.com/ckenaley/JawCloseR). Under this model, the mass component of the lower jaw will be accelerated when the sum of negative and positive torques is positive. The components of the model are described by the following equation:

$$\alpha = \frac{\tau_m + \tau_{d,\text{jaw}} + \tau_{p,\text{jaw}}}{I_{\text{jaw}}}, \quad (1)$$

where α is the angular acceleration of the lower jaw in rad s^{-1}, I_{jaw} is the mass moment of inertia of the lower jaw, and τ_m, $\tau_{d,jaw}$, and $\tau_{p,jaw}$ are torques applied by the jaw adductor muscles and drag and pressure torques acting against the jaw, respectively.

Basic model parameters are summarized here and detailed descriptions of the dynamic jaw-adduction models are provided in the Supplementary Materials and in Kenaley (2012). The model approximates the mass properties of the lower-jaw system by modeling the lower jaw as a half ellipsoid of water that takes the dimensions of the minor and major axes of the jaw rotating about the quadrato-articular joint. Pressure and drag torques were estimated according to the surface area of a half-elliptical plate with the same dimensions in the sagittal and coronal planes of the half ellipsoid representing the mass of the lower jaw. When the lower jaw closes, the intraoral volume will decrease, creating positive pressure that is exerted along the length of the lower jaw. We assumed that oral pressures reached a peak of 200 Pa and that this pressure acted equally along the half-elliptical plate

Table 1
Model parameters and their abbreviations presented in the text and Figs. 1 and 3 .

Abbreviation	Parameter
F_{A_2}	Instantaneous force produced by A_2
F_{A_3}	Instantaneous force produced by A_3
F_{A_ω}	Instantaneous force produced by A_ω
F_{ant}	Minimum component of the series of forces acting parallel with A_ω
F_{disp}	Force of the A_ω normal to the dorsal tip of the Meckelian tendon
F_{res}	Resultant force the A_2 and A_3 divisions
L_{A_ω}	Length and line of action of the A_ω division
L_{A_2}	Length and line of action of the A_2 division
L_{A_3}	Length and line of action of the A_3 division
L_{res}	Theoretical length of the resultant calculated from A_2 and A_3 divisions
$L_{i,a}$	Length of the anterior inlever
$L_{i,p}$	Length of the posterior inlever
L_{oA_2,iA_ω}	Distance between A_2 origin and A_ω insertion
$L_{oA_2,Mt}$	Distance between A_2 origin and Meckelian tendon insertion
L_{oA_2,oA_3}	Distance between A_2 and A_3 origins
$L_{oA_3,Mt}$	Distance between A_3 origin and A_ω insertion
L_{oA_3,iA_ω}	Distance between A_3 origin and Meckelian tendon insertion
L_{ores,oA_3}	Distance between resultant origin ($P_{o,res}$) and A_3 origin (P_{o,A_3})
L_{Mt}	Length to the Meckelian tendon
$L_{Nx,j}$	Distance between the nexus of A_2, A_3, and A_ω and the jaw joint
Mt	Meckelian tendon length and line of action
P_J	Position of jaw joint Cartesian space
$P_{i,Mt}$	Position of the Meckelian insertion on the lower jaw in Cartesian space
P_{Nx}	Position of the shared A_2 and A_3 insertions and A_ω origin on the aponeurosis defining the distal tip of the Meckelian tendon
P_{o,A_2}	Position of A_2 origin in Cartesian space
P_{o,A_2}	Position of A_2 origin in Cartesian space
P_{o,A_3}	Position of A_3 origin in Cartesian space
P_{o,A_ω}	Position of A_ω insertion in Cartesian space
$P_{o,res}$	Theoretical position of the resultant origin between a line defined by P_{o,A_2} and P_{o,A_3}
θ_{A_2,A_3}	Interior angle between A_2 and A_3 lines of action at the aponeurosis (P_{Nx})
θ_{A_2,A_ω}	Exterior angle between A_2 line of action and A_ω line of action
$\theta_{A_2,Mt}$	Exterior angle between A_2 line of action and Meckelian tendon
θ_{A_3,A_ω}	Exterior angle between A_3 line of action and A_ω line of action
$\theta_{A_3,Mt}$	Exterior angle between A_3 line of action and Meckelian tendon
$\theta_{L_{A_2,A_3},A_3}$	Angle between a segment defined by the A_2 and A_3 origins (P_{o,A_2} and P_{o,A_3}) and the A_3 line of action
θ_{A_ω}	Insertion angle of A_ω line of action
$\theta_{A_\omega,Mt}$	Interior angle between the A_ω line of action and the Meckelian tendon
θ_{Mt}	Insertion angle of A_ω line of action
$\theta_{Mt,res}$	Angle between the Meckelian tendon and the line of action between the L_{res}
θ_{res}	Angle of the A_2 and A_3 resultant (L_{res}) relative to the A_2 line of action (L_{A_2})
$\theta_{res,disp}$	The angular displacement of the resultant line of action (L_{res}) due to F_{max,A_ω}

representing the lower jaw. This peak pressure value is much lower than has been assumed in other modeling studies (Van Wassenbergh et al., 2005; de Schepper et al., 2008) reflecting that the oral and opercular chambers of *Chauliodus* are open and quite exposed during feeding (Tchernavin, 1953). Torque applied to the lower jaw by the adductor muscles was calculated according to the length of the inlevers (i.e., distance of attachment to the quadrato-articular joint), angle of the lower jaw (i.e., angle of insertion), and the force produced by the muscles. An estimation of force produced by each muscle in the adductor complex was calculated by its physiological cross-sectional area (PCSA) (Supplementary Equations 2 and 3) and included parameters known to affect muscle-force output, including force-velocity and fiber length-force relationships (Supplementary Equations 4 and 5, respectively), activation rise time (Supplementary Equation 6), and additional parallel elastic forces (Supplementary Equation 7).

Compared to Kenaley (2012), the model implemented in this study differed in two important ways: (1) each origin and insertion landmark on either side of the jaw and suspensorium was projected in 2D coordinates and (2) the geometry and force input of the A_ω division was included in dynamic calculations of jaw adduction. This modified model implements the two-anchor sling configuration and a dynamic relationship of the A_ω with the other divisions. We assumed that the posterior line of the sling (the Meckelian tendon) was a rigid rope. Under this condition, a point formed on the aponeurosis by the A_2 and A_3 insertions and A_ω origin on the Meckelian tendon, or the nexus (*Nx*), was free to rotate about the insertion point of the Meckelian tendon as the jaw rotated and each of the three muscles contracted (Fig. 2). The two-anchor sling configuration results in two input torques at two inlevers: $\tau_{i,a}$, at the anterior inlever ($L_{i,a}$) where A_ω inserts on the lower jaw and $\tau_{i,p}$ at the posterior inlever ($L_{i,p}$) where the Meckelian tendon inserts onto the Meckelian fossa ($P_{i,Mt}$; Fig. 2A). In this configuration, the total muscle torque, τ_m, of Eq. (1) is equal to the sum of $\tau_{i,a}$ and $\tau_{i,p}$.

The amount of torque imparted to the lower jaw at the anterior inlever during each iteration is equal to the minimum component of the series of forces acting parallel with A_ω (i.e., those applied at the aponeurosis by the facialis divisions and by A_ω itself), the sine of the insertion angle of A_ω, and length of the anterior inlever ($L_{i,a}$).

The minimum component of forces acting on the anterior inlever (F_{ant}) was determined by:

$$F_{\text{ant}} = \min(F_{A_2} \times \cos(\theta_{A_2,A_\omega}) + F_{A_3} \times \cos(\theta_{A_3,A_\omega}), F_{A_\omega}), \tag{2}$$

where F_{A_2} and F_{A_3} are instantaneous forces produced by A_2 and A_3, respectively, and θ_{A_2,A_ω} and θ_{A_3,A_ω} are the angles between L_{A_ω} and L_{A_2} and L_{A_3}, respectively. With this, the torque applied to the anterior inlever was calculated as:

$$\tau_{i,a} = L_{i,a} \times \sin(\theta_{A_\omega}) \times F_{\text{ant}}, \tag{3}$$

where θ_{A_ω} is the insertion angle of A_ω on the lower jaw (Fig. 2B) and $L_{i,a}$ is the length of the anterior inlever. θ_{A_ω} was computed as:

$$\theta_{A_\omega} = \cos^{-1}\left(\frac{L_{\text{Mt}}^2 - (L_{i,a} - L_{i,p})^2 - L_{A_\omega}^2}{-2 \times (L_{i,a} - L_{i,p}) \times L_{A_\omega}}\right); \tag{4}$$

and θ_{A_2,A_ω} and θ_{A_3,A_ω} were calculated as:

$$\theta_{A_2,A_\omega} = \cos^{-1}\left(\frac{L_{\text{oA2,iA}_\omega}^2 - L_{A_2}^2 - L_{A_\omega}^2}{-2 \times L_{A_\omega} \times L_{A_2}}\right), \tag{5}$$

and

$$\theta_{A_3,A_\omega} = \cos^{-1}\left(\frac{L_{\text{oA3,iA}_\omega}^2 - L_{A_\omega}^2 - L_{A_3}^2}{-2 \times L_{A_\omega} \times L_{A_3}}\right), \tag{6}$$

respectively, where $L_{\text{oA2,iA}_\omega}$ is the distance between the A_2 origin and A_ω insertion and $L_{\text{oA3,iA}_\omega}$ is the distance between the A_3 origin and A_ω insertion.

The amount of torque applied to the lower jaw at the posterior inlever is equal to the product of the sum of forces parallel with *Mt*, the sine of the insertion angle of *Mt*, and length of the posterior inlever ($L_{i,p}$):

$$\tau_{i,p} = L_{i,p} \times \sin(\theta_{\text{Mt}}) \times (F_{A_2} \times \cos(\theta_{A_2,\text{Mt}}) + F_{A_3} \times \cos(\theta_{A_3,\text{Mt}})), \tag{7}$$

where θ_{Mt} is the insertion angle of the Meckelian tendon onto the lower jaw and $\theta_{A_2,\text{Mt}}$ and $\theta_{A_3,\text{Mt}}$ the angles between the Meckelian tendon and L_{A_2} and L_{A_3}, respectively. θ_{Mt} was computed as:

$$\theta_{\text{Mt}} = \cos^{-1}\left(\frac{L_{\text{Nx},j}^2 - L_{i,p}^2 - L_{\text{Mt}}^2}{-2 \times L_{i,p} \times L_{\text{Mt}}}\right); \tag{8}$$

where $L_{Nx,j}$ is the distance between the *Nx* and the jaw joint. We calculated $\theta_{A_2,\text{Mt}}$ and $\theta_{A_3,\text{Mt}}$ as:

$$\theta_{A_2,\mathrm{Mt}} = \cos^{-1}\left(\frac{L^2_{\mathrm{oA}_2,\mathrm{iMt}} - L^2_{\mathrm{Mt}} - L^2_{A_2}}{-2 \times L_{\mathrm{Mt}} \times L_{A_2}}\right), \tag{9}$$

and

$$\theta_{A_3,\mathrm{Mt}} = \cos^{-1}\left(\frac{L^2_{\mathrm{oA}_3,\mathrm{iMt}} - L^2_{\mathrm{Mt}} - L^2_{A_3}}{-2 \times L_{\mathrm{Mt}} \times L_{A_3}}\right), \tag{10}$$

respectively, where $L_{\mathrm{oA}_2,\mathrm{Mt}}$ and $L_{\mathrm{oA}_3,\mathrm{Mt}}$ are the distances between the insertion point of the Meckelian tendon and the A_2 and A_3 origins respectively (Fig. 2A).

We assumed that, at peak gape, the angle of insertion of the Meckelian tendon would be same as the line of action between the A_2—the strongest muscles division—and the insertion point of the Meckelian tendon (Fig. 2A). Once adduction was initiated, the lines of action and lengths of each muscle at each iteration were determined by the position of the nexus (P_{Nx}), the point of insertion of the A_2 and A_3 and origin of A_ω on the aponeurosis and the distal point of the Meckelian tendon (Fig. 2A). P_{Nx} was calculated by two sequential subiterations. First, the resultant of the forces of the facialias divisions was calculated by finding the angle between the A_2 and A_3 lines of action with reference to the aponeurosis:

$$\theta_{A_2,A_3} = \cos^{-1}\left(\frac{L^2_{\mathrm{oA}_2,\mathrm{oA}_3} - L^2_{A_3} - L^2_{A_2}}{-2 \times L_{A_3} \times L_{A_2}}\right), \tag{11}$$

where $L_{\mathrm{oA}_2,\mathrm{oA}_3}$ is the distance between A_2 and A_3 origins. The resultant F_{res} of the A_2 and A_3 forces acting on the aponeurosis at P_{Nx} (Fig. 2A) was then calculated by:

$$F_{\mathrm{res}} = \sqrt{F^2_{A2} + F^2_{A3} + 2 \times F_{A2} \times F_{A3} * \cos(\theta_{A_2,A_3})}. \tag{12}$$

With this, the resultant angle relative to the A_2 line of action (θ_{res}; Fig. 2A) was then calculated as:

$$\theta_{\mathrm{res}} = \tan^{-1}\left(\frac{F_{A2} \times \sin(\theta_{A_{2,3}})}{F_{A3} + F_{A2} \times \cos(\theta_{A_{2,3}})}\right), \tag{13}$$

The initial angle of the Meckelian tendon for each iteration was assumed to take the line of action of the resultant (Fig. 2A). We thus calculated a theoretical origin for the resultant ($P_{o,res}$) by first finding the angle between the segment defined by the A_2 and A_3 origins (P_{o,A_2} and P_{o,A_3}) and the A_3 line of action (Fig. 2A):

$$\theta_{L_{A_2,A_3},A_3} = \cos^{-1}\left(\frac{L^2_{A_3} - L^2_{A_2,A_3} - L^2_{A_2}}{-2 \times L_{A_2,A_3} \times L_{A_2}}\right), \tag{14}$$

From this, the theoretical length of the resultant as it bisects a line between the A_2 and A_3 origins was calculated as:

$$L_{\mathrm{res}} = \sin(\theta_{L_{A_2,A_3},A_3}) \times \frac{L_{A_3}}{\sin(\mathrm{pi} - \theta_{L_{A_2,A_3},A_3} - \theta_{\mathrm{res}})}, \tag{15}$$

and the distance of this origin between the A_3 and A_2 origins relative to the A_3 origin (Fig. 2A) was thus calculated as:

$$L_{\mathrm{ores,oA}_3} = \sqrt{L^2_{A_3} + L^2_{\mathrm{res}} - 2 \times L_{A_3} * L_{\mathrm{res}} \times \cos(\theta_{\mathrm{res}})}. \tag{16}$$

P_{res} was then calculated as the point of intersection between L_{res} and L_{res,A_3} given θ_{res} (Fig. 2A).

At each iteration, the tension of A_ω will exert some displacement on the line of action formed by the facialis resultant (L_{res}) and Meckelian tendon (Fig. 2B). To invoke this, we modeled the resultant length and tendon as a two-chord assembly joined in series and under a perpendicular displacing force F_{disp} from the A_ω at their union (Fig. 2B). The chord L_{res} was free to change length between its origin and insertion at the aponeurosis as if the tension of the chord was applied about a pulley at $P_{o,res}$ (Fig. 2C). The perpendicular displacing force was calculated as:

$$F_{\mathrm{disp}} = F_{A_\omega} \times \sin(\theta_{A_\omega,\mathrm{Mt}}), \tag{17}$$

where $\theta_{A_\omega,\mathrm{Mt}}$ is the angle between the A_ω line of action and the Meckelian tendon (Fig. 2B). $\theta_{A_\omega,\mathrm{Mt}}$ was calculated by:

$$\theta_{A_\omega,\mathrm{Mt}} = \cos^{-1}\left(\frac{(L_{i,a} - L_{i,p})^2 - L^2_{A_\omega} - L^2_{M_t}}{-2 \times L_{A_\omega} \times L_{M_t}}\right). \tag{18}$$

The force F_{disp} will result in a disrupted line of action between the L_{res} and the Meckelian tendon and some angle between these two cords, $\theta_{Mt,res}$ (Fig. 2C) that is determined by the proportion of F_{disp} relative to F_{res}, or:

$$\theta_{\mathrm{Mt,res}} = \pi - \sin^{-1}\left(\frac{F_{\mathrm{disp}}}{F_{\mathrm{disp}} + F_{\mathrm{res}}}\right). \tag{19}$$

The resultant line of action was displaced an angle $\theta_{res,disp}$, a value calculated with the law of sines using $\theta_{Mt,res}$ and the combined length of the two cords L_{Mt} and L_{res}, and the undisplaced line of action (Fig. 2C):

$$\theta_{\mathrm{res,disp}} = \sin^{-1}\left(\frac{\theta_{\mathrm{Mt,res}} \times L_{\mathrm{Mt}}}{L_{\mathrm{Mt}} + L_{\mathrm{res}}}\right). \tag{20}$$

According to the angle of the Meckelian tendon as determined by the facialis resultant and displacing force of A_ω, P_{Nx} was thus determined and, based on this point, each muscle length and line of action was then calculated. The length of the facialis divisions, L_{A_2} and L_{A_3}, were calculated as the distance between P_{Nx} and P_{o,A_2} and P_{o,A_3}, respectively, where P_{o,A_2} and P_{o,A_3} are the positions of the A_2 and A_3 origins, respectively.

2.3. Jaw-closing simulations

The explicit goal of simulations was to evaluate adduction performance under three different conditions. First, jaw adduction was simulated with the two-anchor sling configuration in place. In a second set of simulations, we followed Kenaley (2012) by ignoring the two-anchor configuration, but accounting for the mass of A_ω by adding it to the mass of the A_2 division for PCSA calculations. In a third set of simulations, we ignored the A_ω altogether and permitted only the facialis divisions to impart torque on the lower jaw via the Meckelian tendon.

Adduction simulations were performed under the three scenarios described above for each of the ten specimens of *C. sloani*. Model input accorded to the values of biometric data presented in Table S1. Simulations were performed with a time step of 0.1 ms and iterated until the jaw was closed to a gape angle of 5°. At the beginning of jaw adduction ($t = -0.1$ to $t = 0$ ms), jaw acceleration was set to 0 rad s^{-1}. To avoid circularity, angular acceleration was computed at each time step based upon the values for the angular velocity and jaw angle from the previous time step ($t - 0.1$ ms). The maximum gape angle was set to 110° according to analyses by Tchernavin (1953). For all simulations, it was assumed that all three adductor muscles began contraction simultaneously at $t = 0$ with a geometry depicted in Fig. 2A (i.e., that the A_2 forms a straight line of action with A_ω).

After initial model runs with the two-anchor sling configuration in place, we found that the position of the nexus at each iteration was very sensitive to the dynamics of facialis and A_ω input, especially during a phase of jaw adduction when the A_ω line of action approaches a position normal to the line of action formed by the facialis resultant (L_{res}) and Meckelian tendon (Fig. 2B). This often resulted in considerable and biologically irrelevant changes in facialis and A_ω muscle lengths which, in turn, resulted in oscillating high and low magnitudes of force production due to the model's implementation of the Hill equation (Hill, 1938). To stabilize the nexus position, we simply constrained the normalized force production according to the force–velocity relationship to equal the average of this parameter over the previous 2 ms (see below). This resulted in more biologically relevant muscle length changes and velocities for all three divisions. We recognize this is an artificial constraint and that future models should include more sophisticated neuromechanical feedback mechanisms that may stabilize these

components.

To assess the contribution of the A_ω to adduction dynamics, three variables were analyzed from model outputs: time to full jaw adduction, maximum angular velocity, and static bite force. We compared the effect of the three model configurations on these metrics using two-way ANCOVAs with specimen mass as a covariate and configuration as a factor and performing subsequent post-hoc Tukey's multiple comparison test. Results were considered significant at a $p < 0.05$ level.

To assess how the A_ω affects facialis muscle posture and dynamics, we also analyzed the following output variables as they varied over jaw closing: insertion angle of the Meckelian tendon, total effective transmission of muscle force (EMA), changes in total mass-specific muscle torque and mass-specific muscle torque at the Meckelian tendon, changes in the force-length (F_{FL}) and force-velocity (F_{FL}) factors for each facialis division, and power output of the two facialis divisions.

EMA, a measure of the amount of effective force per unit muscle force (Biewener, 1989), was calculated with:

$$\mathrm{EMA} = \frac{F_{\mathrm{out}}}{\Sigma F_{\mathrm{max}}}, \tag{21}$$

where F_{out} is the static force output at the jaw tip and ΣF_{max} is the total amount of in-line force produced by the adductor muscles.

F_{FL} is the proportion of normalized force that can be produced given the relationship between muscle fibre length (FL) and an optimal FL (FL_o) which results in maximal force production (see Supplementary Equation 5). We assumed that FL_o would be reached at muscle lengths according to a jaw position at 25% closed.

Muscle power (P, in watts) was calculated as:

$$P = F \times V, \tag{22}$$

where F is the instantaneous force (in Newtons) and V the instantaneous velocity (in m s^{-1}) of each facialis division. Mass-specific P in W kg^{-1} was calculated by dividing this value by muscle mass.

The amount of power produced by a muscle during shortening is largely dependent on the Hill equation (Hill, 1938). This relationship predicts that peak muscle power is optimized at intermediate relative muscle shortening velocities (V/V_{max}, where V is the instantaneous shortening velocity and V_{max} is the maximum shortening velocity Rome and Alexander, 1990; Askew and Marsh, 1998). V_{max} was set to 15 ML s^{-1}, a value corresponding to the fast, white trunk musculature of fishes (Van Leeuwen et al., 1990). A modified Hill model is represented in our study as a force-velocity factor (F_{FV}, Supplementary Equation 4), the proportion of normalized force produced (P/P_o) across a range of velocities. We report F_{FV} values to assess whether the A_ω alters facialis muscle power by modulating the shortening velocity of these divisions. We also report instantaneous muscle velocity (in ML s^{-1}) and relative shortening velocities (V/V_{max}) to evaluate the direct role the A_ω has in altering these parameters and muscle power output.

Lastly, we portrayed the difference in muscle geometry and closing duration for each modeled scenario in a single specimen (MCZ 42217, 25.8 mm SL) in a series of three videos (Supplementary Files Videos S1–S3). Muscle insertions, Meckelian tendon insertion, and the position of the nexus on the aponeurosis were superimposed on an outline of the head and oral jaw system over 1 ms intervals until the jaw was closed.

3. Results

3.1. Muscle geometry and dynamics

Including the A_ω had the effect of increasing the insertion angles of the Meckelian tendon and much more effective transmission of the resultant forces of the adductor system (Fig. 3A and B, Videos S1–S3). This was indicated by the substantially increased total amount of torque imparted to the lower jaw, especially over the first half of jaw adduction when total torque increased as much as much as four times relative to models not fully implementing A_ω (Fig. 3D). Together, the more anterior displacement of facialis muscle forces and tendon angle closer to 90° resulted in a two-fold increase of EMA from early in jaw closing and nearly an eight-fold increase in the later two-thirds (Fig. 3B). This effect was seen despite a considerable reduction of torque input at the Meckelian tendon (Fig. 3C). A model fully implementing A_ω geometry and mass predicted that the A_ω does not substantially change the lengths of the facialis divisions during adduction and therefore does little to change the force-length relationship of the facialis divisions (Fig. 4).

Patterns of instantaneous muscle velocity, force, and power for both facialis divisions are substantially different between the fully implemented model and those simulations not including the A_ω (Fig. 5). Much higher magnitudes of concentric muscle-shortening velocities are attained in the model implementing the A_ω sling (Fig. 5A and B). This results in a lower production of normalized force under our implementation of the Hill relationship (Fig. 5C and D). While total normalized force peaks at around 30% closed and decreases thereafter for all simulations, inclusion of the A_ω sling results in an overall reduction of total normalized force for both facialis divisions as compared to simulations ignoring the A_ω (Fig. 5E and F). This, in turn, contributes to an overall trend of higher A_2 and A_3 power over the first half of adduction and reduced power over the second half of adduction in simulations including the A_ω sling compared to simulations not including the A_ω. Muscle power for the A_2 and A_3 peaks at around 95 and 110 W kg^{-1}, respectively, just before 40% adduction in the fully implemented model and a peak of around 100 W kg^{-1} at 60% closed for both divisions in the alternative models (Fig. 5G,H). Simulations including the A_ω sling result in higher A_2 and A_3 power over the first half of adduction and reduced power over the second half of adduction as compared to simulations not including the A_ω.

3.2. Jaw-closing dynamics

Throughout adduction, lower-jaw angular velocity was greatest in the model that fully implemented A_ω mass and geometry versus the two that did not, especially after approximately 25% closed (Fig. 6A). Peak angular acceleration was greatest in the fully implemented model at over twice the value as the other models, although considerable deceleration was predicted later in adduction (Fig. 6B). A fully implemented model also resulted in significant changes in adduction duration, static bite force, and maximum angular velocity (ANCOVA: $F = 26.3$, $p < 0.0001$, $F = 49.05$, $p < 0.0001$, and $F = 56.1$, $p < 0.0001$, respectively; Fig. 7). Accounting for the A_ω mass and geometry resulted in significantly decreased adduction duration compared to simulations with the A_ω mass added to the A_2 and those completely ignoring the division (Tukey: both $p < 0.0001$). Similarly, simulations implementing A_ω geometry and mass resulted in increased predicted static bite force versus the alternative model excluding the A_ω geometry and a model excluding mass and geometry (Tukey: both $p < 0.0001$). Maximum angular velocity was also significantly higher in the fully implemented model compared to simulations adding the A_ω mass added to the A_2 and a model ignoring both A_ω mass and geometry (Tukey: both $p < 0.001$; Fig. 7).

The two model configurations that did not include A_ω geometry predicted very similar closing dynamics, with only very modest changes in dynamics predicted by the models. Both incomplete models predicted nearly identical profiles of angular velocity and acceleration during adduction, with peak velocity at approximately 60% (Fig. 6A) and peak acceleration at approximately 40% (Fig. 6B). Simulations in which the A_ω mass was added to the A_2 mass predicted an insignificantly small decrease in adduction time (Tukey: $p = 0.61$) and insignificant increases in maximum static bite force and angular velocity (Tukey: $p = 0.92$ and $p = 0.76$, respectively; Fig. 7).

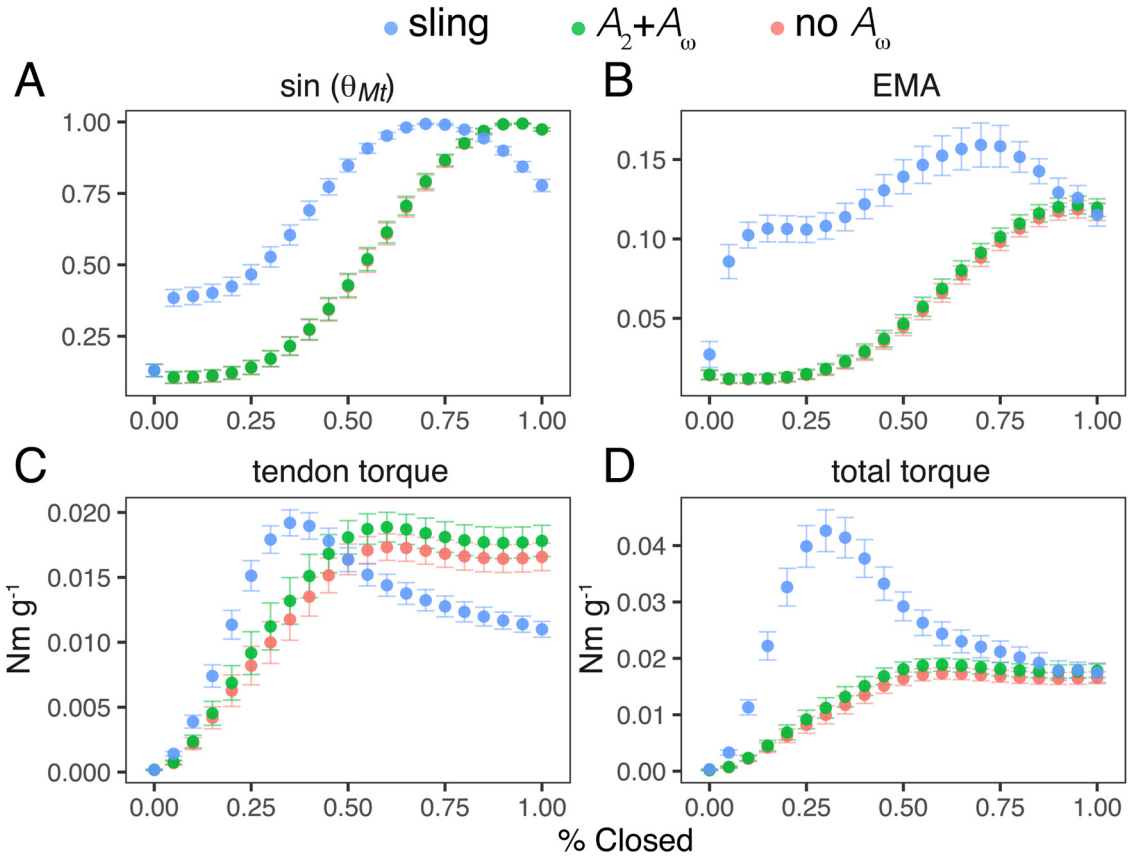

Fig. 3. Mean model output depicting changes in muscle posture, effective transmission of muscle force, and jaw-closing torques: (A) sine of the insertion angle of the Meckelian tendon (θ_{Mt}); (B) effective mechanical advantage (EMA); (C) mass-specific torque imparted through the Meckelian tendon at the posterior inlever; (D) total mass-specific muscle torque imparted to the lower jaw. Note that sine θ_{Mt} and EMA are dimensionless. "Sling," in blue points, represents output when A_ω geometry and mass was fully implemented in the model. "A_2 + A_3," in green points, represents output when A_ω geometry were completely ignored and A_ω mass was added to A_2 for PCSA calculations; "no A_ω," in red points, represents output when both A_ω mass and geometry were completely ignored. Whiskers represent ± 1 standard error.

4. Discussion

4.1. A_ω influence on muscle dynamics and closing performance

Our simulations predict that the A_ω adds substantially to lower-jaw adduction dynamics in *C. sloani*. The input of the A_ω acts to displace the line of action of the A_2 and A_3 muscles (Fig. 3A and B, Videos S1–S3). In so doing, the application of adductor forces on the lower jaw is shared between the more posterior insertion of the Meckelian tendon and the anterior insertion of the A_ω. Thus, a share of muscle input force is imparted to a longer inlever resulting in a greater effective mechanical advantage (Fig. 3B).

Vertebrate muscles function in diverse roles during locomotion as motors, springs, struts and breaks (Dickinson et al., 2000). The role of muscles during feeding has been universally characterized as a motor. By finding that the A_ω is capable of changing the lines of action of the facialis divisions and directing their input to a different point along the jaw inlever, we suggest another important function of vertebrate muscles as a steering motor, directing force generated by other muscles. Future modeling and experimental work should evaluate the capability of muscles in similarly complex feeding and locomotor systems to guide the force output of other linked segments.

By imparting force on a longer inlever, the A_ω increases the mechanical advantage (MA) of the lower jaw system. This increase would, under a simple model of lever dynamics, result in the classic tradeoff of sacrificing adduction velocity for higher output force. In this sense, computing MA has often been used as a means to predict jaw-closing performance (Westneat, 2004; Grubich et al., 2008; Maie et al., 2009). These and other studies have suggested that low inlever–outlever ratios (i.e. low MAs) facilitate relatively high jaw displacement and fast adduction at the expense of force transmission. We show in this study that removing an input force—the A_ω—to a more posterior position by adding the mass of this division to the A_2 will result in slower adduction and reduced velocities. Kenaley (2012) used a similar model to demonstrate that shortening input moment arms in other members of the family Stomiidae also resulted in slower adduction. This and our results suggest that, because of large resistive forces involved in rotating a jaw through a viscous medium, relatively greater MA may be required to accelerate the mass of the lower jaw and maintain velocity while the jaw experiences significant drag.

Other modeling studies of the lower-jaw system in fishes suggest that the position of muscle insertion on the lower jaw is constrained by relatively high resistive forces, especially drag and pressure, that scale exponentially with jaw length (Van Wassenbergh et al., 2005; de Schepper et al., 2008). In an approach similar to this study and Kenaley's (2012) adjustment of MA in the stomiid lower jaw system, McHenry (2012) modeled higher gearing ratios in the linkages of the mantis shrimp (*Gonodactylus smithii*) raptorial appendage. By shortening an input link in the four-bar linkage system that drives the shrimp's appendage and thereby increasing the kinematic transmission (KT, the ratio of change in output versus input angle), McHenry (2012) found that the appendage achieved a lower maximum velocity and acceleration compared to a system modeled with a lower KT value and gearing ratio. Thus, interpretations of the performance of biomechanical systems based on morphometric data alone (i.e., ignoring the effects of movement through a viscous medium) may obscure the

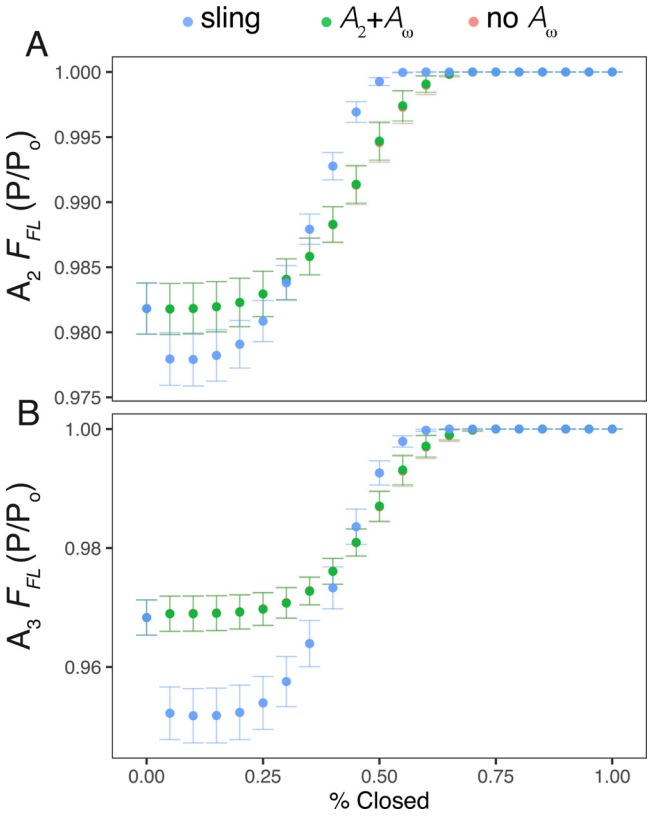

Fig. 4. Model output of mean force-fiber length factor (F_{FL}) for the (A) A_2 and (B) A_3 divisions throughout jaw adduction. "Sling," in blue points, represents output when A_ω geometry and mass (i.e., PCSA) was fully implemented in the model. "A_2 + A_3," in green points, represents output when A_ω geometry was completely ignored and A_ω mass was added to A_2 for PCSA calculations; "no A_ω," in red points, represents output when both A_ω mass and geometry were completely ignored. F_{FL} is the proportion of normalized force (P/P_o) that can be produced given the relationship between muscle fibre length (FL) and an optimal FL (FL_o) which results in maximal force production. Whiskers represent ± 1 standard error.

relationships between mechanics and movement dynamics in aquatic organisms.

While the A_ω configuration may increase jaw closing speed relative to non-sling configurations, it does so without sacrificing output force. By adding an input moment arm of greater length, the A_ω adductor sling increases the EMA of the lower-jaw system. Aside from the advantages of greater acceleration and increased velocity due to increased EMA, the more effective application of force by the A_ω results in the lower jaw traversing the gape with greater bite force more quickly. This is especially advantageous for species with larger gape angles, like species of the family Stomiidae, whose gapes exceed 120° (Kenaley, 2012). If a prey item is encountered early in adduction, the effect of the sling configuration increases the likelihood that the prey item would be immobilized.

Our results indicate that a lower-jaw system with the A_ω achieves higher closing performance—including jaw velocity, static bite force, and adduction time (Fig. 7)—with substantially different applications of muscle power (Fig. 5G and H). An A_ω-based system results in considerably higher outputs of facialis power over the first half of adduction and a reduced output of power over the second half. This is due to a more effective application of muscle force (Fig. 3B) which results in elevated instantaneous adduction velocities throughout closing (Fig. 6A). Higher adduction velocity, in turn, results in relatively higher muscle-shortening velocities for the A_2 and A_3 and consequently a shift along their respective force-velocity curves and a commensurate reduction in normalized force output (Fig. 5C and D). Due to his force-velocity relationship, vertebrate muscles produce power optimally at intermediate shortening velocities, typically around 0.1–0.4 V/V_{max} (Rome and Alexander, 1990; Askew and Marsh, 1998). Over the first half of closing, contractile velocities maintain intermediate values at around 2–6 ML s^{-1} (0.13–0.4 V/V_{max}), thereby optimizing power output. However, in the second half of adduction, contractile velocities exceed these intermediate values at over 7.5 ML s^{-1} (> 0.5 V_{max}; Fig. 5A and B) and power is reduced compared to the simulations that ignore the A_ω (Fig. 5G and H). Due to a less effective application of muscle force and slower adduction velocities in simulations that do not implement the A_ω, intermediate muscle-shortening values are not reached until late in adduction, delaying peak A_2 and A_3 power (Fig. 5G and H).

4.2. Importance of the A_ω system to deep-sea species

In addition to clear performance advantages, we have revealed through our alternative simulations that an investment of PCSA is more fully optimized in the A_ω system than in the facialis divisions alone. By simply adding the mass of the A_ω to the facialis components, we have simulated the development of hypertrophic facialis components of the adductor system, a strategy that several groups of fishes have undertaken to increase bite force and reduce adduction time (Turingan and Wainwright, 1993; Herrel et al., 2002). Relative to simulations in which this mass is ignored, this investment in the facialis components results in only very marginal increases in bite force and closing velocity (Fig. 7). If PCSA is invested in the A_ω system, adduction performance is increased substantially. This indicates that, to achieve both a stronger and faster bite, an investment of any amount of PCSA in the adductor system is more effective if it is made in the A_ω system. This could be especially important in the deep-sea where food resources are especially limited and therefore the assimilation and maintenance of metabolically expensive muscle mass is particularly challenging. A system that increases the effectiveness of delivering a more forceful and quicker bite with a relatively modest investment in PCSA can be seen as an adaptation to the food limitations in the deep sea and indicates perhaps why this configuration is common in so many predatory groups that inhabit this ecosystem (Datovo and Vari, 2013).

Furthermore, the jaws of dragonfishes are extremely long and gracile. The large resistive forces of drag and pressure, but also the inertia and drag imparted by any large prey item, may impose deformation to the delicate bones of the lower jaw. By applying an anteriorly displace moment, the A_ω may stabilize these skeletal elements and reduce this deformation.

4.3. The A_ω and analogous systems in other vertebrates

While our results demonstrate the important contributions of the A_ω sling to the viperfish and other deep-sea fishes, the prevalence of this configuration throughout the teleost tree of life (Datovo and Vari, 2013) suggests that this is an important component of lower-jaw adduction in many other groups. Whether the A_ω sling imparts similar postural changes and performance advantages in other fishes should be evaluated either through similar modeling approaches, *in-vivo* experimentation, or even robotic feeding models (Kenaley and Lauder, 2016). Until additional comparative work is undertaken, elucidating the role of a sling-type configuration in lower-jaw adduction may require looking to work focussed on the cartilago transiliens (CT) system in archosaur tetrapods. The cartilago transiliens of crocodilians is an intramuscular, sesamoid element composed of fibrocartilage that serves as a point of insertion for two jaw adductors: the more anterior pseudotemporalis superficialis muscle and posterior adductor mandibulae externus profundus (Tsai and Holliday, 2011). Additional fibers of the adductor mandibulae externus profundus insert ventrally on the coronoid process of the mandible. The ventral aspect of the cartilago transiliens is the site of origin for the intramandibularis which, just as the A_ω of many

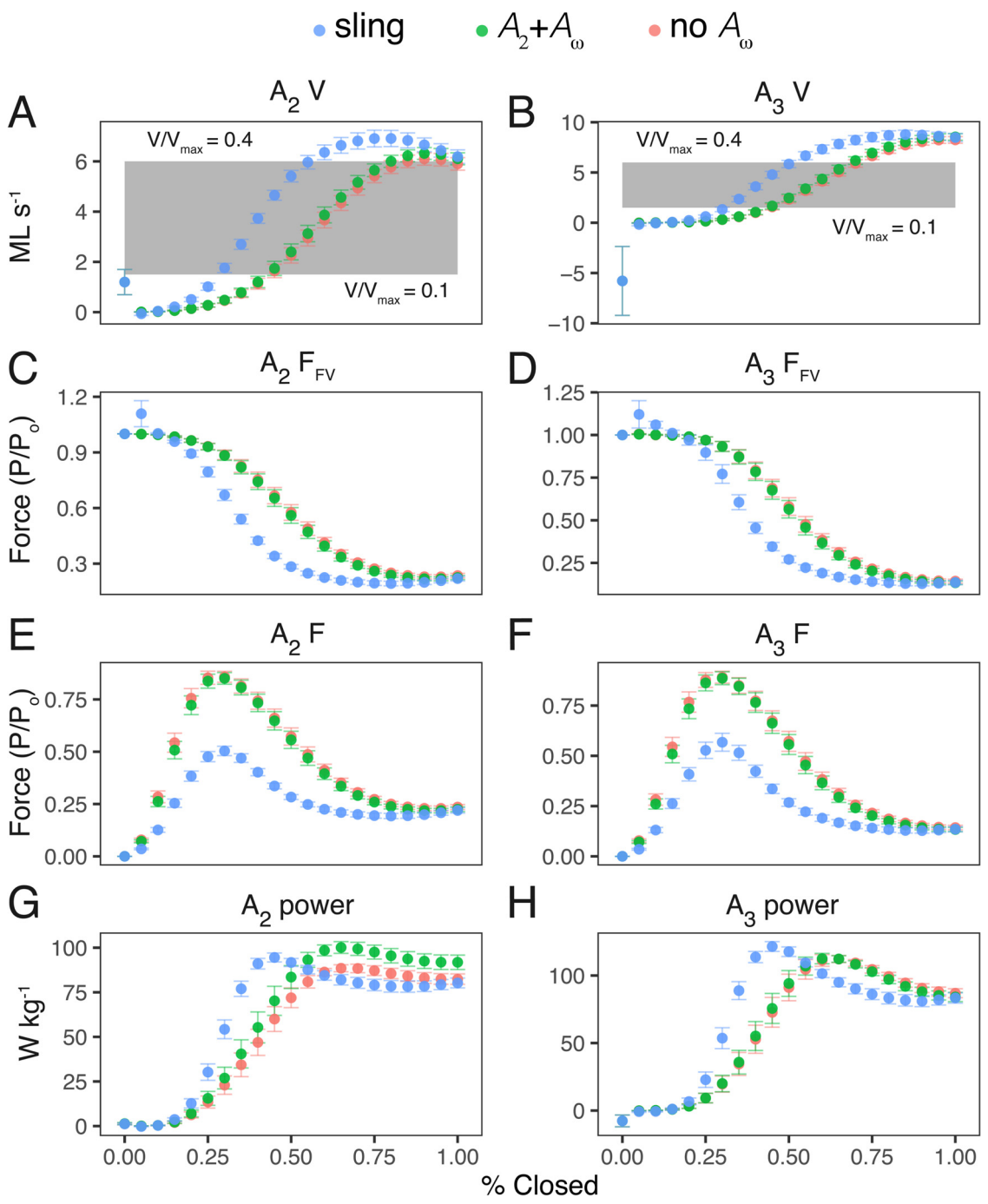

Fig. 5. Mean model output depicting facialis muscle velocity, normalized force, and power between three simulations over jaw adduction: (A) and (B) A_2 and A_3 velocity (in muscle lengths s^{-1}); (C) and (D) A_2 and A_3 normalized force (P/P_o) production according to the model force–velocity relationship; (E) and (F) total normalized force produced by A_2 and A_3; (G) and (H) A_2 and A_3 power. Grey boxes in A and B correspond to intermediate values of V/V_{max} between 0.1 and 0.4. Muscle power is reported as work rate divided by muscle mass (in kg) to give muscle-mass specific values. "Sling," in blue points, represents output when A_ω geometry and mass was fully implemented in the model. "A_2 + A_3," in green points, represents output when A_ω geometry was completely ignored and A_ω mass was added to A_2 for PCSA calculations; "no A_ω," in red points, represents output when both A_ω mass and geometry were completely ignored. Whiskers represent ± 1 standard error.

teleosts, inserts within the Meckelian fossa (Tsai and Holliday, 2011).

The cartilago transiliens thus forms a nexus of adductor divisions that constitutes a geometry very similar to that of the A_ω sling in *C. sloani* and many other fishes, with two points of insertion on the lower jaw and two dorsal origins on the head. Whether the cartilago transiliens could change input dynamics as we have described for a viperfish has received little scientific attention. Busbey (1989) considered whether the cartilago transiliens system of *Alligator mississippiensis* could displace adductor moments to a more anterior position and concluded that this was unlikely because activation of the intramandibularis occurs intermittently and not synchronously in the adductor mandibulae externus profundus. Schumacher (1973) asserted that the intramandibularis of crocodilians pulls the CT anteroventrally, thereby lengthening the adductor mandibulae externus profundus and pseudotemporalis superficialis and thus altering their positions along their respective length–tension curves. This limited work on the CT suggests

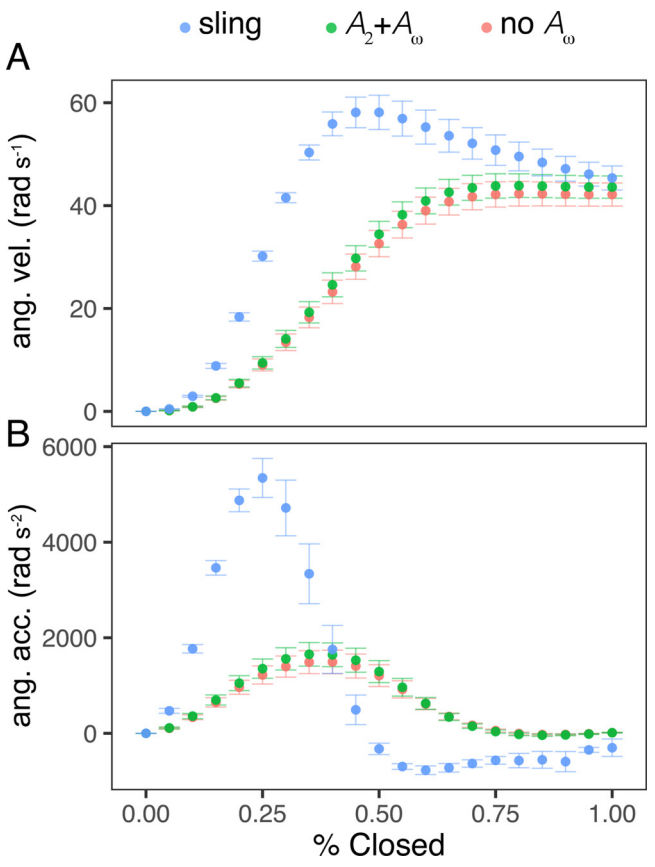

Fig. 6. Model output for (A) mean angular velocity and (B) mean angular acceleration over jaw closing: "Sling," in blue points, represents output when A_ω geometry and mass (i.e., PCSA) was fully implemented in the model. "A_2 + A_3," in green points, represents output when A_ω geometry was completely ignored and A_ω mass was added to A_2 for PCSA calculations; "no A_ω," in red points, represents output when both A_ω mass and geometry were completely ignored. Whiskers represent ± 1 standard error.

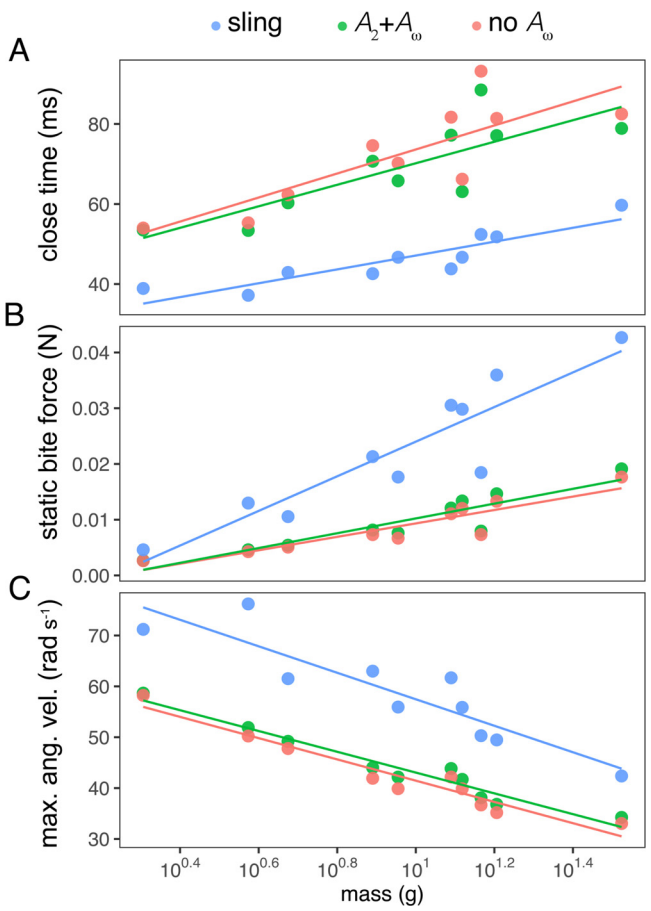

Fig. 7. Model output for (A) adduction duration, (B) maximum static bite force, and (C) maximum angular velocity in three simulations. "Sling," in blue points, represents output when A_ω geometry and mass (i.e., PCSA) was fully implemented in the model. "A_2 + A_3," in green points, represents output when A_ω geometry was completely ignored and A_ω mass was added to A_2 for PCSA calculations; "no A_ω," in red points, represents output when both A_ω mass and geometry were completely ignored.

that, in contrast to the A_ω system, a similar sling arrangement may indeed be important in modulating force-length properties of large dorsal adductors. This would seem to require asynchronous activation of the dorsal and intramandibular components. The simulations invoked in our study assumed simultaneous activation of all adductors. Future modeling of the adductor system in fishes should include variation in muscle activation, perhaps based on *in-vivo* EMG patterns, to assess whether such variation could modulate force–length properties as well.

Finally, we note that the precise effects of the A_ω systems on input moments and muscle dynamics in teleosts would be more fully elucidated if modeling studies such as this were coupled with electromyographic studies of live specimens. Although this is an impossible approach for deep-sea species, EMG studies of shallow-water taxa with similar A_ω architecture (e.g., *Esox*; Winterbottom, 1973) will be important in understanding whether variation in activation patterns contributes to adduction dynamics. Alternatively, researchers may assess the importance of this parameter through the design of physical, biorobotic models that mimic adductor architecture and permit manipulations of motor patterns.

Author contributions

CPK helped conceive the study, wrote the code responsible for simulations, performed the analysis, and wrote the manuscript. MR helped conceive the study, took morphological data, and wrote the manuscript. GVL helped conceive the study, performed analysis, and wrote the manuscript.

Acknowledgements

This study was funded with a National Science Foundation Postdoctoral Fellowship in Biology awarded to CPK (Award Number 1103761). We wish to thank members of the Lauder lab for their helpful discussion and the MCZ for use of their imaging facility. Two anonymous reviewers provided valuable critiques to that helped improve the manuscript.

Appendix A. Supplementary data

Supplementary data associated with this article can be found, in the online version, at https://doi.org/10.1016/j.zool.2019.02.005.

References

Askew, G.N., Marsh, R.L., 1998. Optimal shortening velocity (V/Vmax) of skeletal muscle during cyclical contractions: length–force effects and velocity-dependent activation and deactivation. J. Exp. Biol. 201, 1527–1540.

Biewener, A.A., 1989. Scaling body support in mammals: limb posture and muscle mechanics. Science 245, 45–48.

Busbey, A.B., 1989. Form and function of the feeding apparatus of *Alligator mississippiensis*. J. Morphol. 202, 99–127.

Clarke, T.A., 1982. Feeding habits of stomiatoid fishes from Hawaiian waters. US Fish. Bull. 80, 287–304.

Datovo, A., Vari, R.P., 2013. The jaw adductor muscle complex in teleostean fishes: evolution, homologies and revised nomenclature (Osteichthyes: Actinopterygii). PLoS One 8, e60846.
Dickinson, M.H., Farley, C.T., Full, R.J., Koehl, M., Kram, R., Lehman, S., 2000. How animals move: an integrative view. Science 288, 100–106.
Fink, W.L., 1985. Phylogenetic interrelationships of the stomiid fishes (Teleostei: Stomiiformes). Misc. Publ. Mus. Zool. Univ. Mich. 171, i–vii 1–127.
Gibb, A., 1995. Kinematics of prey capture in a flatfish, *Pleuronichthys verticalis*. J. Exp. Biol. 198, 1173–1183.
Grubich, J.R., Huskey, S., Crofts, S., Orti, G., Porto, J., 2012. Mega-bites: extreme jaw forces of living and extinct piranhas (Serrasalmidae). Sci. Rep. 2, 1009.
Grubich, J.R., Rice, A.N., Westneat, M.W., 2008. Functional morphology of bite mechanics in the great barracuda (*Sphyraena barracuda*). Zoology 111, 16–29.
Herrel, A., Adriaens, D., Verraes, W., Aerts, P., 2002. Bite performance in clariid fishes with hypertrophied jaw adductors as deduced by bite modeling. J. Morphol. 253, 196–205.
Herring, P.J., 2002. Biology of the Deep Ocean. Oxford University Press, Oxford.
Hill, A.V., 1938. The heat of shortening and the dynamic constants of muscle. Proc. R. Soc. Lond. B 126, 136–195.
Kenaley, C.P., 2012. Exploring feeding behaviour in deep-sea dragonfishes (Teleostei: Stomiidae): jaw biomechanics and functional significance of a loosejaw. Biol. J. Linn. Soc. 106, 224–240.
Kenaley, C.P., DeVaney, S.C., Fjeran, T.T., 2014. The complex evolutionary history of seeing red: molecular phylogeny and the evolution of an adaptive visual system in deep-sea dragonfishes (Stomiiformes: Stomiidae). Evolution 68, 996–1013.
Kenaley, C.P., Lauder, G.V., 2016. A biorobotic model of the suction-feeding system in largemouth bass: the roles of motor program speed and hyoid kinematics. J. Exp. Biol. 219, 2048–2059.
Lauder, G.V., 1980. Evolution of the feeding mechanism in primitive actionopterygian fishes: a functional anatomical analysis of *Polypterus*, *Lepisosteus*, and *Amia*. J. Morphol. 163, 283–317.
Lauder, G.V., Norton, S.M., 1980. Asymmetrical muscle activity during feeding in the gar, *Lepisosteus oculatus*. J. Exp. Biol. 84, 17–32.
Maie, T., Schoenfuss, H.L., Blob, R.W., 2009. Jaw lever analysis of Hawaiian gobioid stream fishes: a simulation study of morphological diversity and functional performance. J. Morphol. 270, 976–983.
McHenry, M.J., 2012. When skeletons are geared for speed: the morphology, biomechanics, and energetics of rapid animal motion. Integr. Comp. Biol. 52, 588–596.
Metscher, B.D., 2009. MicroCT for comparative morphology: simple staining methods allow high-contrast 3D imaging of diverse non-mineralized animal tissues. BMC Physiol. 9, 11.
R Core Team, 2018. R: A Language and Environment for Statistical Computing. R Foundation for Statistical Computing, Vienna, Austria. URL: https://www.R-project.org/.
Rome, L.C., Alexander, R.M., 1990. The influence of temperature on muscle velocity and sustained performance in swimming carp. J. Exp. Biol. 154, 163–178.
de Schepper, N., Van Wassenbergh, S., Adriaens, D., 2008. Morphology of the jaw system in trichiurids: trade-offs between mouth closing and biting performance. Zool. J. Linn. Soc. 152, 717–736.
Schnell, N.K., Britz, R., Johnson, G.D., 2010. New insights into the complex structure and ontogeny of the occipito-vertebral gap in barbeled dragonfishes (Stomiidae, Teleostei). J. Morphol. 271, 1006–1022.
Schnell, N.K., Johnson, G.D., 2017. Evolution of a functional head joint in deep-sea fishes (Stomiidae). PLoS One 12, e0170224.
Schumacher, G.H., 1973. The head muscles and hyolaryngeal skeleton of turtles and crocodilians. Biol. Reptil. 4, 101–200.
Sutton, T.T., Hopkins, T.L., 1996. Trophic ecology of the stomiid (Pisces: Stomiidae) fish assemblage of the eastern gulf of mexico: strategies, selectivity and impact of a top mesopelagic predator group. Mar. Biol. 127 179-192-192.
Tchernavin, V.V., 1953. The Feeding Mechanisms of a Deep sea Fish, *Chauliodus sloani* Schneider. British Museum of Natural History, London.
Tsai, H.P., Holliday, C.M., 2011. Ontogeny of the alligator cartilago transiliens and its significance for sauropsid jaw muscle evolution. PLoS One 6, e24935.
Turingan, R.G., Wainwright, P.C., 1993. Morphological and functional bases of durophagy in the queen triggerfish, *Balistes vetula* (Pisces, Tetraodontiformes). J. Morphol. 215, 101–118.
Van Leeuwen, J., Lankheet, M., Akster, H., Osse, J., 1990. Function of red axial muscles of carp (*Cyprinus carpio*): recruitment and normalized power output during swimming in different modes. J. Zool. 220, 123–145.
Van Wassenbergh, S., Aerts, P., Adriaens, D., Herrel, A., 2005. A dynamic model of mouth closing movements in clariid catfishes: the role of enlarged jaw adductors. J. Theor. Biol. 234, 49–65.
Wainwright, P.C., McGee, M.D., Longo, S.J., Patricia Hernandez, L., 2015. Origins, innovations, and diversification of suction feeding in vertebrates. Integr. Comp. Biol. 55, 134–145.
Wainwright, P.C., Richard, B.A., 1995. Predicting patterns of prey use from morphology of fishes. Environ. Biol. Fish. 44, 97–113.
Westneat, M.W., 2004. Evolution of levers and linkages in the feeding mechanisms of fishes. Integr. Comp. Biol. 44, 378–389.
Westneat, M.W., 2005. Skull biomechanics and suction feeding in fishes. Fish Physiol. Series 23, 29–75.
Winterbottom, R., 1973. A descriptive synonymy of the striated muscles of the teleostei. Proc. Acad. Natl. Sci. Phila. 125, 225–317.